Supplement of Atmos. Chem. Phys., 23, 7611–7633, 2023
https://doi.org/10.5194/acp-23-7611-2023-supplement

Atmospheric Chemistry and Physics
Open Access
EGU

Supplement of

Investigating the vertical extent and short-wave radiative effects of the ice phase in Arctic summertime low-level clouds

Emma Järvinen et al.

Correspondence to: Emma Järvinen (emma.jaervinen@kit.edu)

S1 Habit classification scheme for PHIPS stereo-images

In the literature of the past few decades, various habit classification schemes for ice crystals and snowflakes have been proposed. One of the earliest and most comprehensive schemes was presented by Nakaya and Sekido in 1936 (Nakaya and Sekido, 1936), which categorized snowflakes into seven main groups with 26 subcategories in total. Kikuchi et al. (2013) proposed a more detailed version with as many as 121 categories divided into eight main categories. In recent years, Bailey and Hallett's habit diagram has gained popularity and is often cited (Bailey and Hallett, 2009).

We use a classification scheme based on Bailey and Hallett's habit diagram, which distinguishes between single crystals and polycrystals, with columnar and plate-like subsections, each including several habits. We have made some modifications to the scheme, such as excluding rarely observed habits (i.e. spearheads and Gohei twins) and adding frequently observed ones, such as capped columns and mixed rosettes.

One notable difference between our scheme and Bailey and Hallett's is that we differentiate between ice crystal habits and attributes, which can be related to any habit. Attributes such as hollowness, air inclusions, riming, and aggregation are considered. For example, instead of using the habit categories hollow column and solid column, we assign the habit column and the attribute hollow to a hollow column.

To sort the habit classes, we use a tree-like structure, with the main node distinguishing between single, polycrystals, and graupel. The next level subdivides into plate-like, column-like, and mixed growth. The leaf nodes are the specific habits, such as plate, sectored plate, skeletal plate, dendrite, column, needle, bullet, side plane, bullet rosette, needle rosette, capped column, capped bullet rosette, and mixed rosette. In addition to ice crystal habits, we also classify droplets and differentiate between frozen and liquid ones. An illustration of this classification scheme is shown in figure S1.

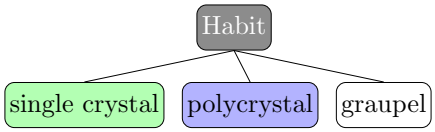

(a) Habit categories

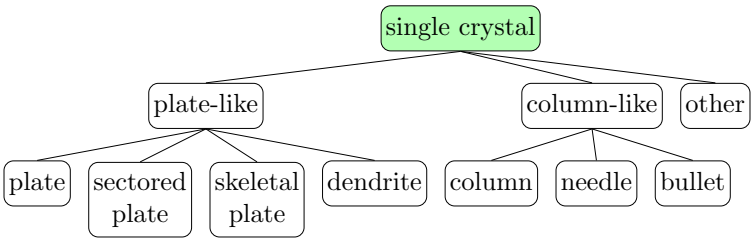

(b) Habit categories: single crystal branch

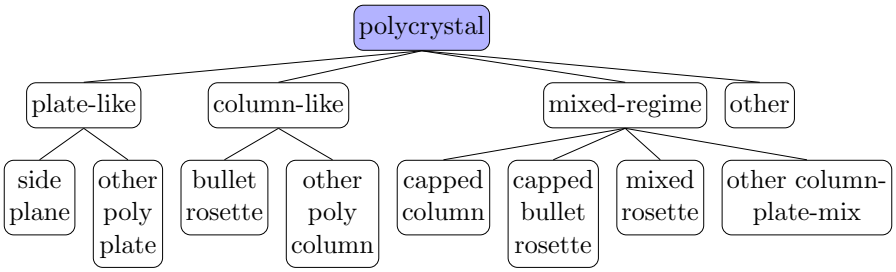

(c) Habit categories: polycrystal branch

Figure S1: manual classification system

Our habit categories cover the classes of ice particles proposed by Kikuchi et al. (2013) as follows:

- Plate: P1a, P1b, R1b, R2b, G2a, G2b
- Sectored plate: P2a, P2b, P4f, G2c
- Skeletal plate: P1c
- Dendrite: P3a-P3c, P4a-P4e, P4g, R1c, R2c, R2d
- Column: C2a, C2b, C3a-C3d, R1a, R2a, G1a
- Needle: C1a-C1c
- Bullet: C4a-C4c
- Other single crystal: CP6a, G1b, G3a, G3b
- Sideplane: P7a, P7b, CP4c, R1d
- Other poly plate: P6a-P6d, P8b, CP4a, CP4b, CP7a, CP7c, CP7e, CP7g, G4a-G4c
- Bullet rosette: C4d
- Other poly column: C2c, C3e, CP7d

- Capped column: CP1a-CP1c, CP2a, CP2b
- Capped bullet rosette: CP2c, CP2d
- Mixed rosette: CP7b, CP8b
- Other column-plate-mix: CP3a-CP3f, CP5a, CP6e, CP6f, CP8a, CP8c, CP8d, CP9a-CP9e
- Other polycrystal: CP6a-CP6d, CP6g, CP6h, CP7f, H2a
- Graupel: R3a-R3c, R4a-R4c

Depending on the image quality, crystal size and orientation, classification is done to the level where it can clearly be determined. When a polycrystal cannot be assigned to a specific habit, but the growth direction is detectable, it falls into one of the following categories: other poly plate, other poly column or other column-plate mix. When the growth direction of a polycrystal is not detectable, it will be classified as other polycrystal. Example PHIPS images of each habits are displayed in figure S2 to S17. Since not all habits have been sampled during the ACLOUD campaign, some example images from the CIRRUS at High-Latitude (CIRRUS-HL) campaign, that took place in 2021, and Investigation of Microphysics and Precipitation for Atlantic Coast-Threatening Snowstorms (IMPACTS) deployment in 2022.

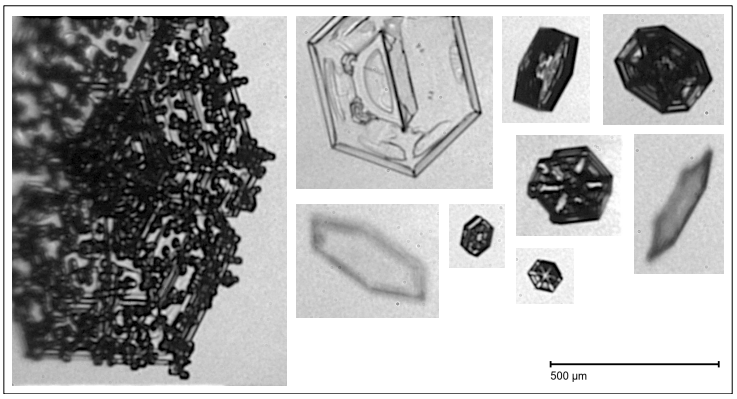

Figure S2: Plate examples, images from the ACLOUD campaign

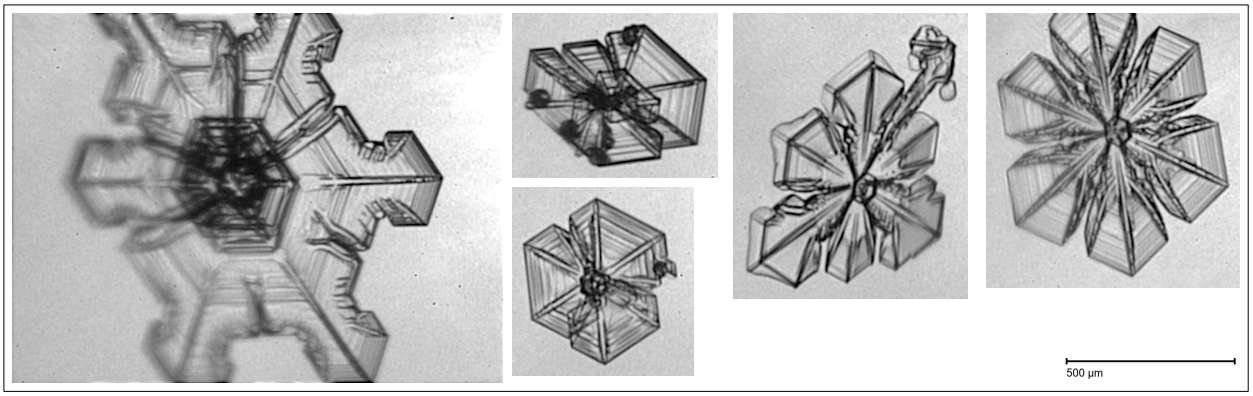

Figure S3: Sectored plate examples, images from the ACLOUD campaign

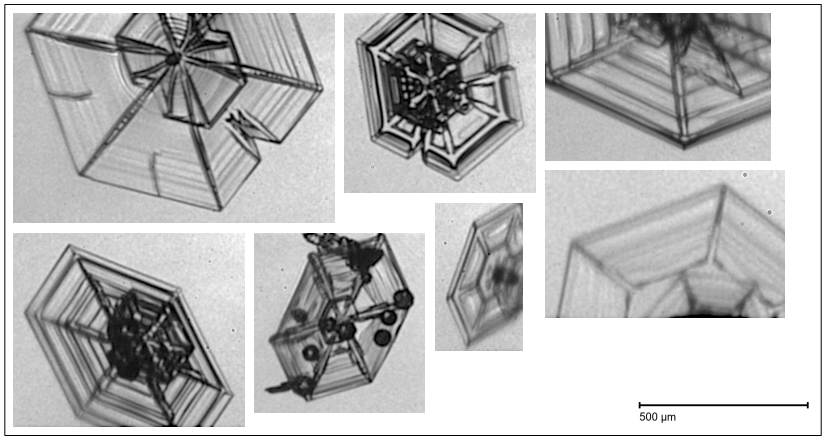

Figure S4: Skeletal plate examples, images from the ACLOUD campaign

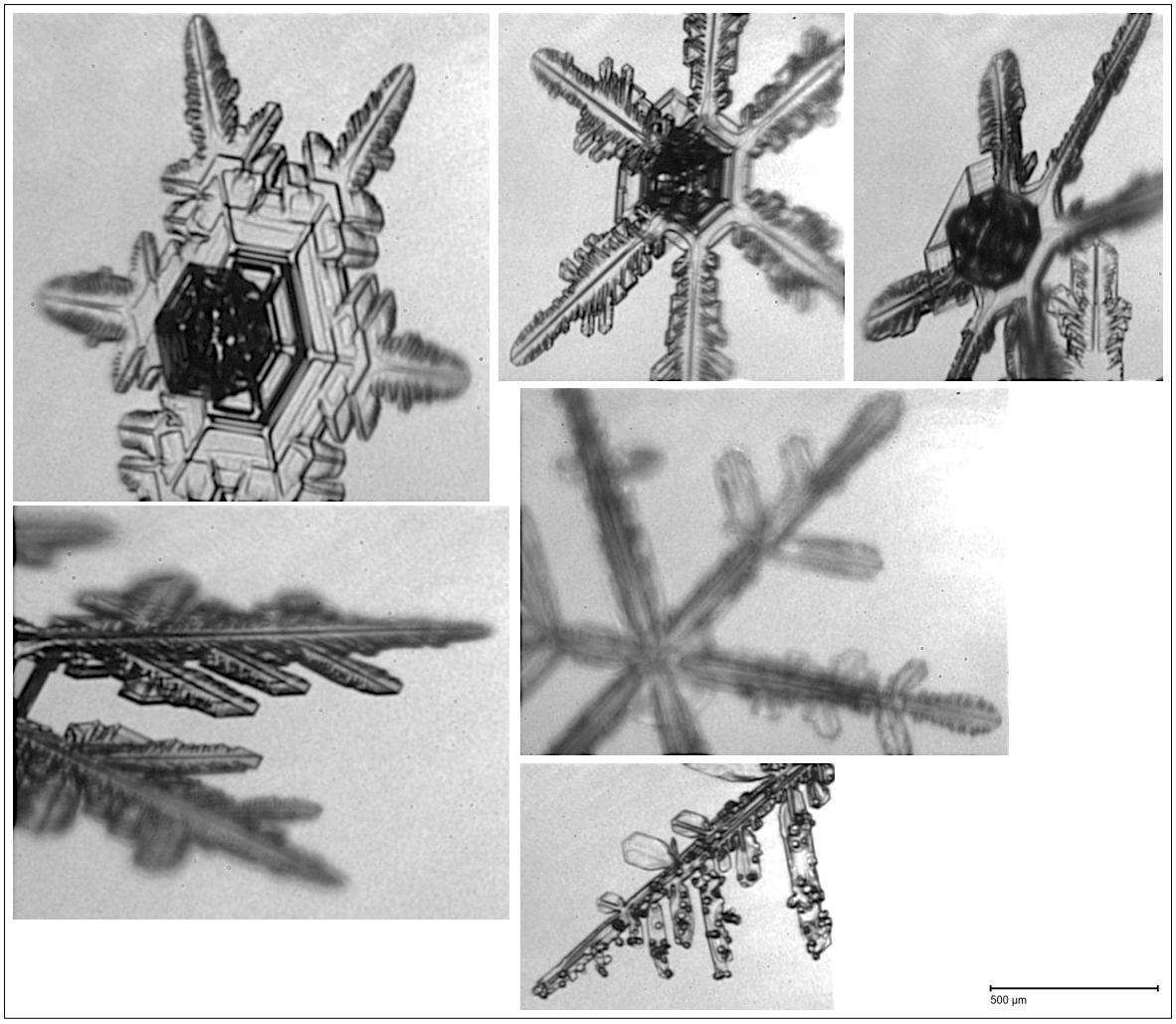

Figure S5: Dendrite examples, images from the ACLOUD campaign

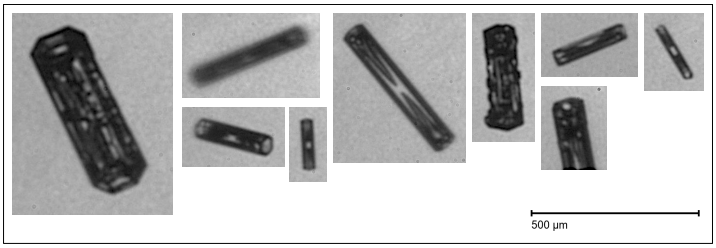

Figure S6: Column examples, images from the ACLOUD campaign

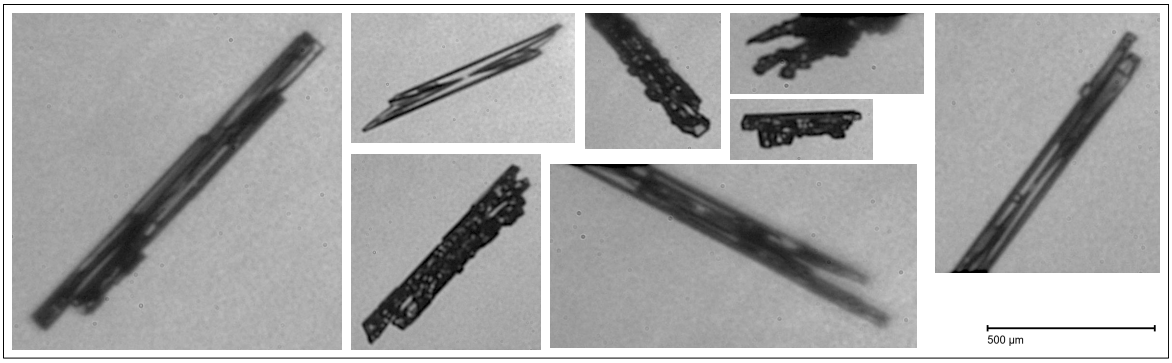

Figure S7: Needle examples, images from the ACLOUD campaign

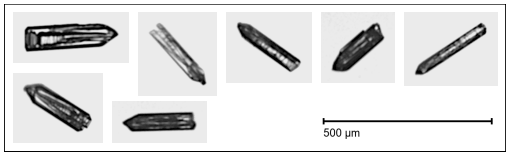

Figure S8: Bullet examples, images from the CIRRUS-HL campaign

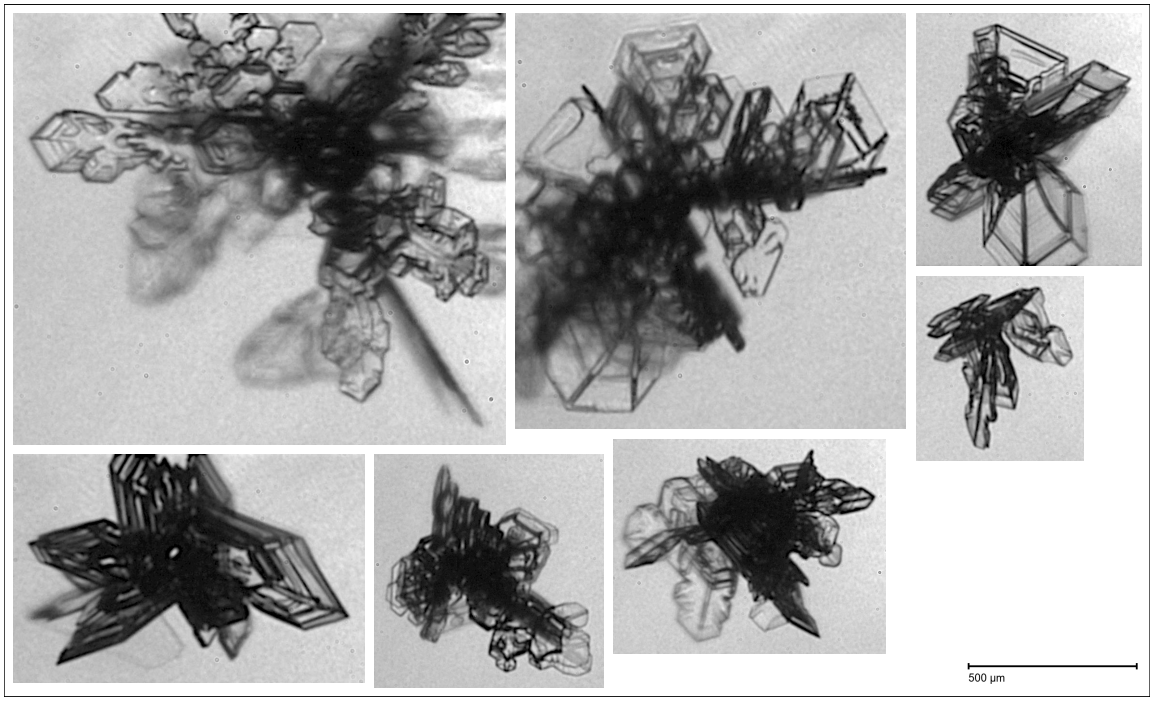

Figure S9: Sideplane examples, images from the ACLOUD campaign

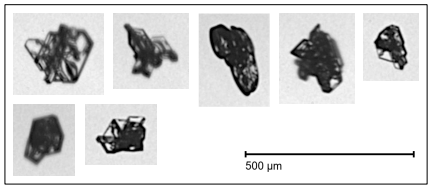

Figure S10: Other poly plate examples, images from the CIRRUS-HL campaign

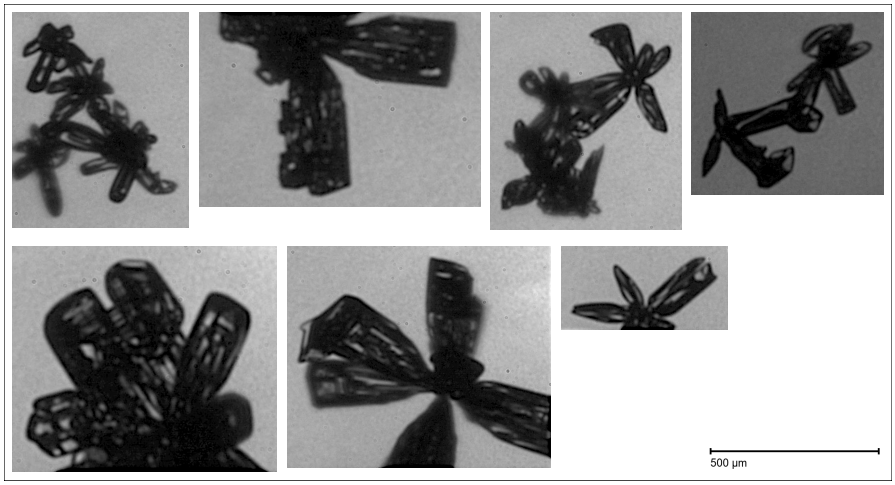

Figure S11: Bullet rosette examples, images from the ACLOUD campaign

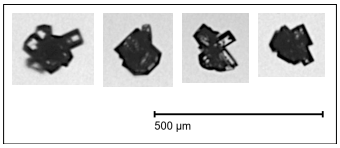

Figure S12: Other poly column examples, images from the CIRRUS-HL campaign

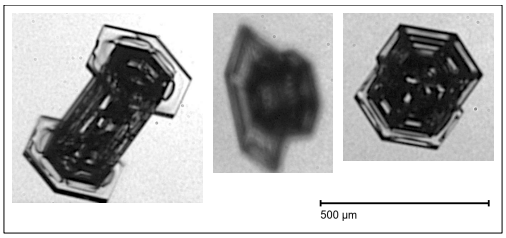

Figure S13: Capped column examples, images from the ACLOUD campaign

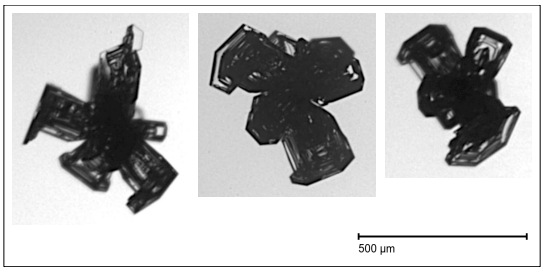

Figure S14: Capped bullet rosette examples, images from the IMPACTS campaign

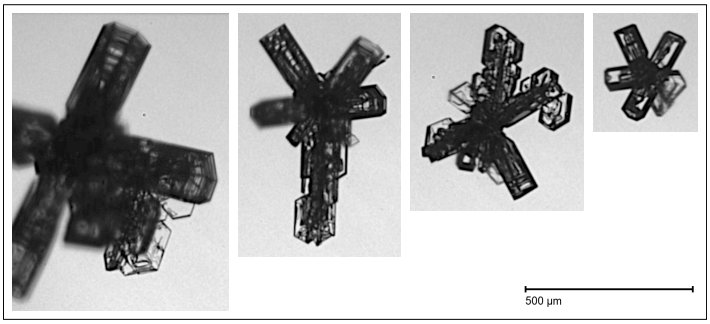

Figure S15: Mixed rosette examples, images from the CIRRUS-HL campaign

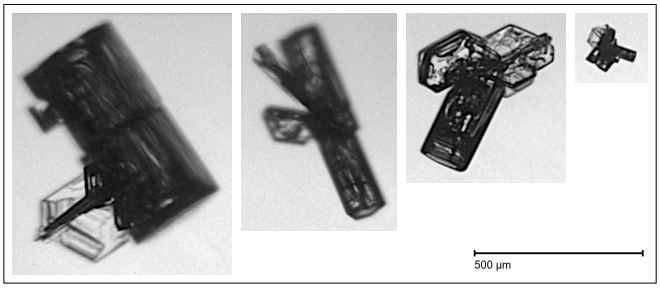

Figure S16: Other column-plate-mix examples, images from the CIRRUS-HL campaign

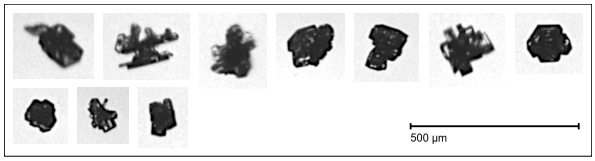

Figure S17: Other polycrystal examples, images from the CIRRUS-HL campaign

In addition to its habit, we assign the following, optional attributes to the PHIPS ice crystal images:

- Shattering
- Multiple particles
- Aggregate
- Chain aggregate
- Rimed
- Pristine
- Sublimating
- Air inclusion
- Hollow
- Dendritic growth
- Atypical facet angle

S2 Sensitivity of IWC to different mass-dimensional relations

Retrieving bulk microphysical properties, like IWC, from measurements of ice crystal size or projected area requires assumptions on the relationships between the masses and lengths of ice particles. A general approach in the literature has been to relate the length of an ice crystal to its mass using the following equation

$$M(L) = aL^b, \tag{S1}$$

where $M(L)$ is the mass, L length and a, b constants. The constants a and b are usually determined from measurements of L and M of ice crystals collected at ground sites (e.g. Mitchell et al., 1990) or from simultaneous measurements of particle size distributions and IWC with total water probe (e.g. Brown and Francis, 1995; McFarquhar et al., 2007).

The choice of the mass-dimensional (M-D) relation used can significantly impact the estimated magnitude of IWC. In this section, we investigate the sensitivity of the retrieved IWC to the assumed M-D relation. We consider three M-D relations: the widely used Brown and Francis (1995) relation (hereafter BF95), McFarquhar et al. (2007) relation (hereafter M07), and the Lawson and Baker (2006) relation (hereafter LB06). The BF95 relation was obtained in cirrus clouds during two flights, raising concerns about its applicability to mixed-phase cloud ice crystals. In contrast, the M07 relation was obtained for mixed-phase clouds during the M-PACE campaign. The LB06 relation is a revision of Mitchell et al.'s (1990) work, in which precipitation ice crystals were collected and their habits, as well as their length and mass, were determined. The LB06 relation includes habit-dependent M-D relations, with plates, needles, and rimed needles being the relevant habits for the clouds measured during ACLOUD.

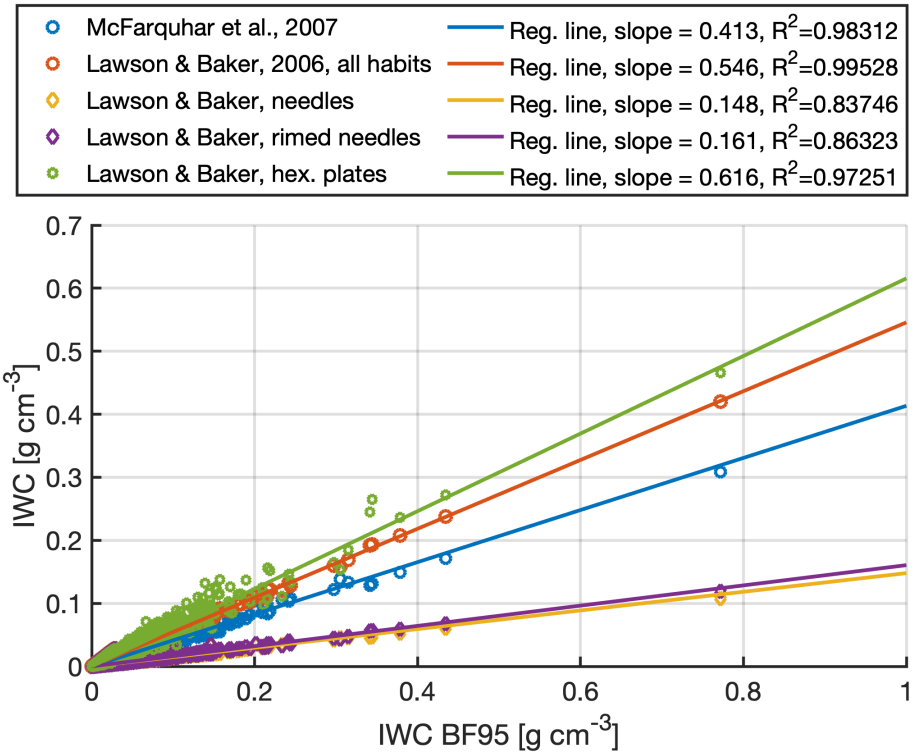

Figure S18: Comparison of IWC retrieved using BF95 and M07 (blue), LB06 all habits (red), LB06 needles (yellow), LB06 rimed needles (purple) and LB06 hexagonal plates (green). Lines show the results of linear regression without intercept.

Figure S18 shows the results of the IWC comparison between BF95 and other M-D relationships. It can be seen that compared to BF95, M07 and LB06 relations for all habits and hexagonal plates predict lower IWCs by 40 to 60%. The lowest IWCs (by around 85% compared to BF95) are predicted by LB06 assuming needles and rimed needles. This highlights the difficulty of retrieving bulk ice microphysical properties, like mass, from measurements of ice crystal dimensions.

S3 Calculation of averaged cloud vertical profiles

The vertical profiles of liquid and ice phase microphysical properties were measured by sampling the clouds using horizontal legs at different altitudes. Typically, three to five different altitudes were sampled during one cloud profile. To calculate the average vertical profile, we used 10-second cloud microphysical observations and divided them into equidistant vertical bins. For each bin, we calculated the mean and standard deviation. Since the number of vertical altitude bins used for the calculation of the average profiles was typically larger than the number of horizontal legs, some altitude bins contain better statistics than others. This is illustrated in Figures S19 to **??** which show the flight pattern and the 10-second LWC and IWC observations as a function of altitude, together with the altitude bin limits applied to calculate the mean and standard deviation shown in Figures 3, 4, 6, 7, 10, and 12.

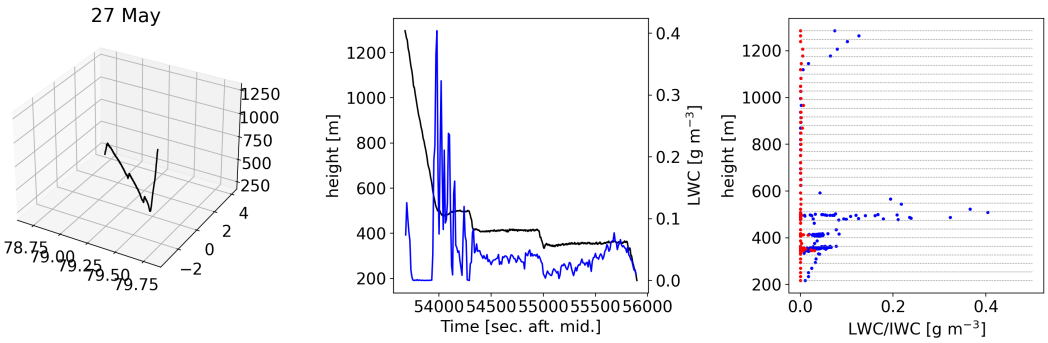

Figure S19: Vertical profile performed on 27 May. The first panel shows an illustration of the flight pattern as a function of latitude, longitude and height. The second panel shows time series of the altitude (black) and LWC (blue). The third panel shows 10-second average LWC (blue) and IWC (red) observations as a function of altitude. The grey lines illustrate the altitude bin edges used to calculate statistics.

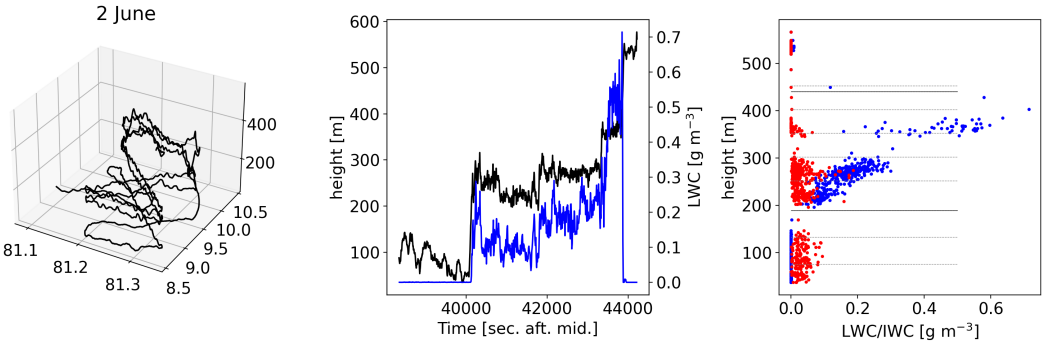

Figure S20: Vertical profile performed on 2 June. The first panel shows an illustration of the flight pattern as a function of latitude, longitude and height. The second panel shows time series of the altitude (black) and LWC (blue). The third panel shows 10-second average LWC (blue) and IWC (red) observations as a function of altitude. The grey lines illustrate the altitude bin edges used to calculate statistics. The darker lines illustrate the cloud top and base used for calculation of the normalised altitude.

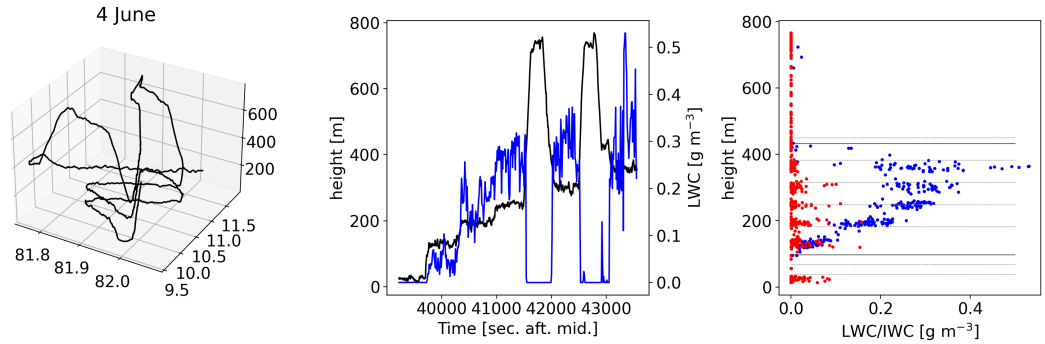

Figure S21: Same as Fig. S20 but for 4 June.

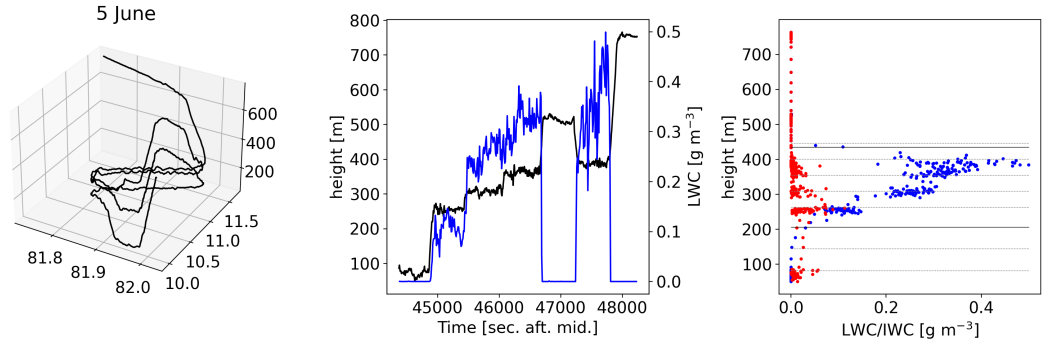

Figure S22: Same as Fig. S20 but for 5 June.

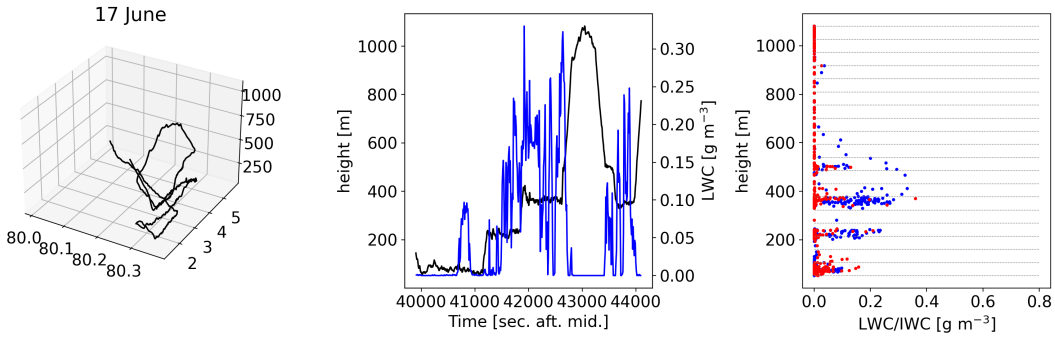

Figure S23: Same as Fig. S19 but for 17 June.

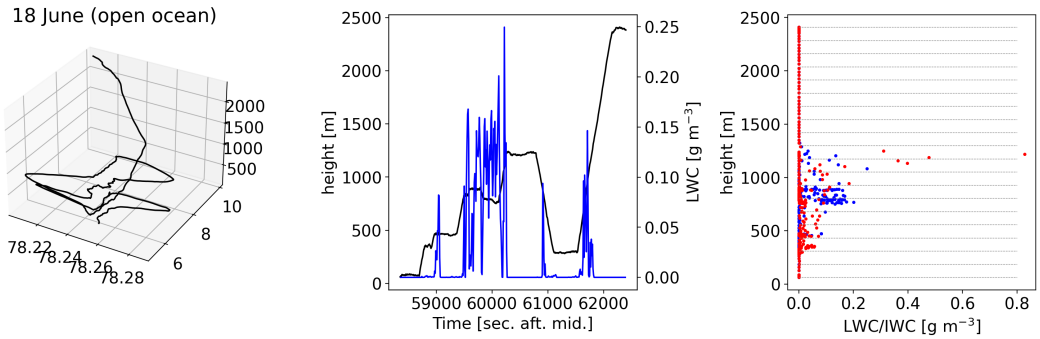

Figure S24: Same as Fig. S19 but for 18 June.

S4 Particle size distributions measured during vertical profiles

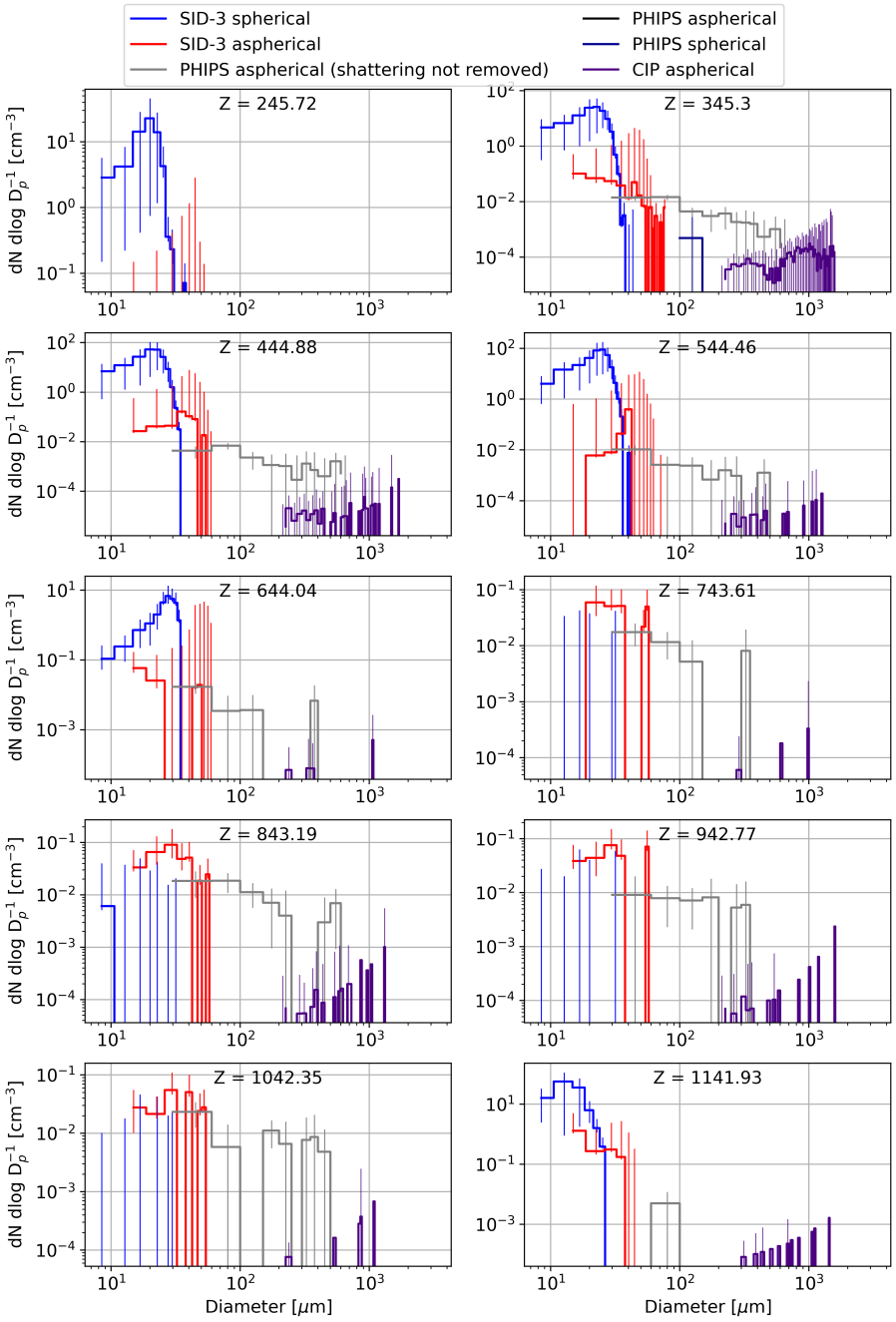

Figure S25: Phase separated particle size distributions for different altitudes (Z) measured during cloud sampling on 27 May. Each sub-plot represents the particle size distributions that are averaged over two height bins, where Z is the bin mean height in meter. The vertical error bars represent the statistical uncertainty. Note that PHIPS and SID-3 aspherical particles were excluded from analysis of ice concentration, ice effective diameter, IWC and ice extinction coefficient due to shattering artefacts.

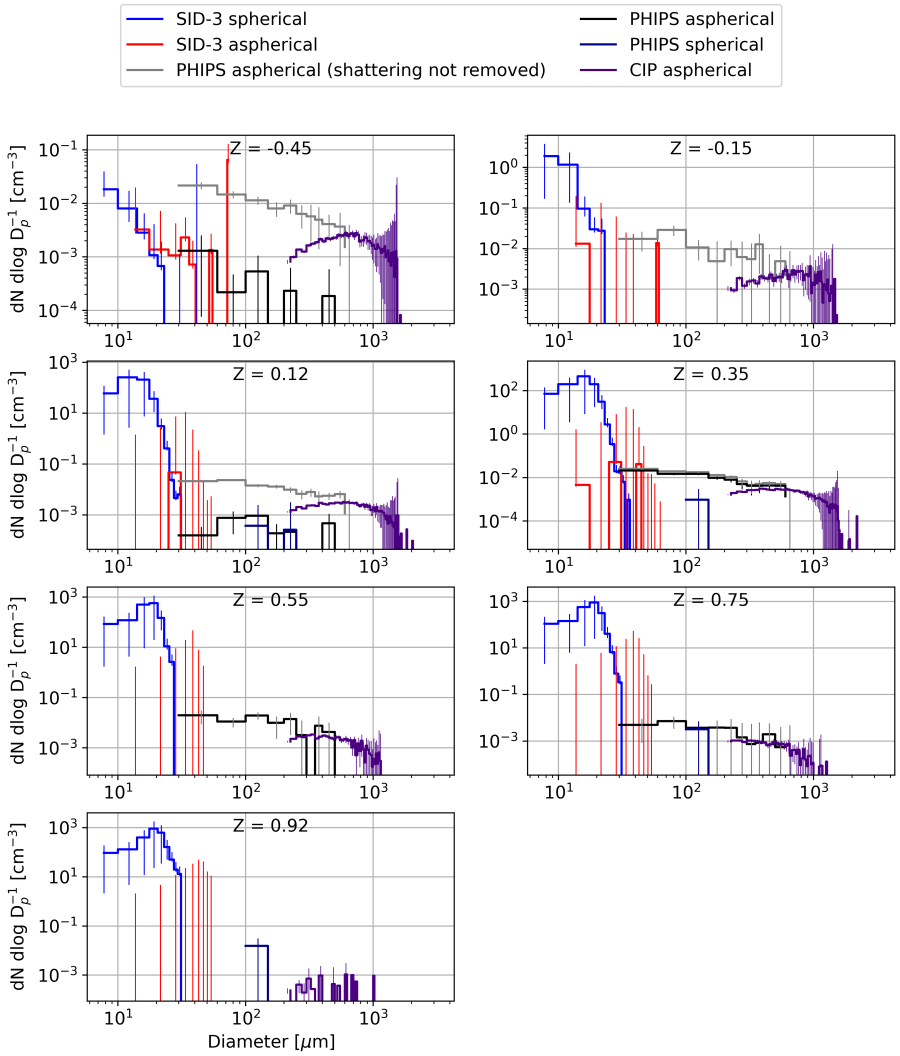

Figure S26: Phase separated particle size distributions for different normalised altitudes (Z) measured during cloud sampling on 2 June. Each sub-plot represents the particle size distributions that are averaged over one normalised altitude bin, where Z is the bin mean normalised altitude. The vertical error bars represent the statistical uncertainty. Periods with shattering artifacts are identified in PHIPS aspherical concentrations with grey color and for these periods the ice concentration, ice effective diameter, IWC and ice extinction coefficient are calculated only using CIP.

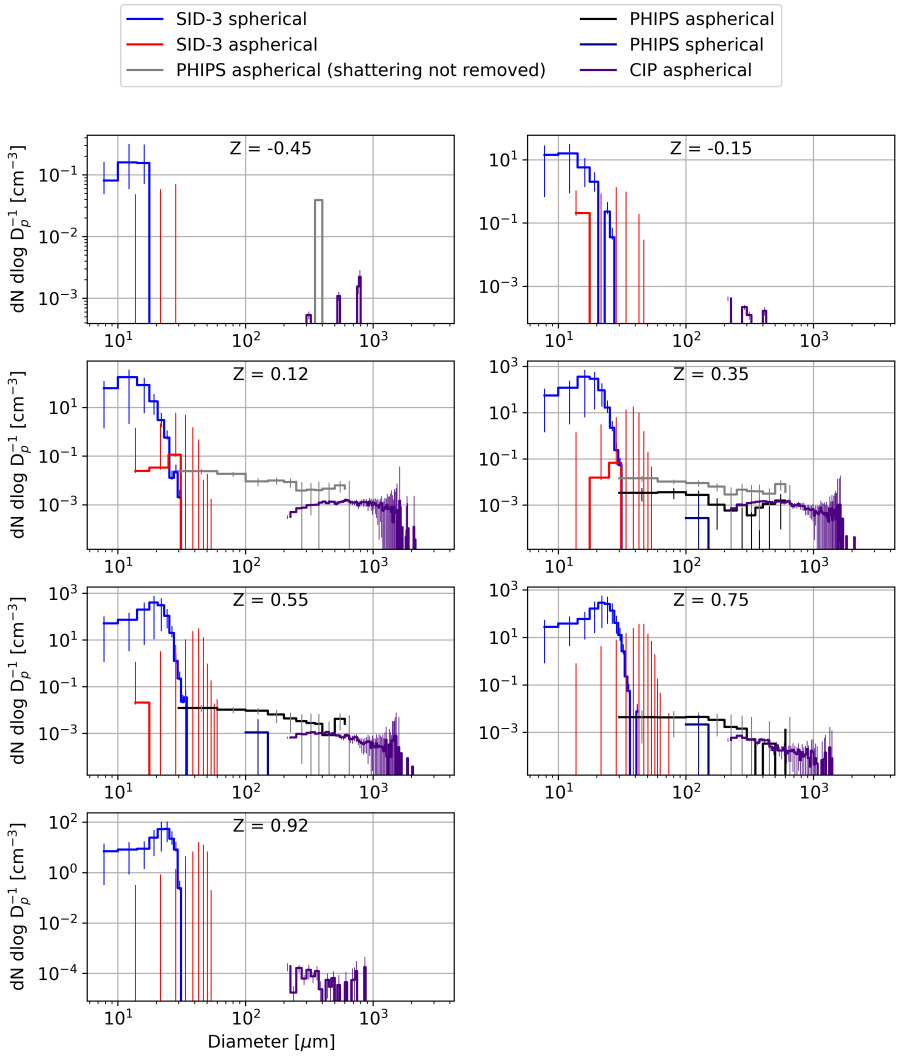

Figure S27: Phase separated particle size distributions for different normalised altitudes (Z) measured during cloud sampling on 4 June. Each sub-plot represents the particle size distributions that are averaged over one normalised altitude bin, where Z is the bin mean normalised altitude. The vertical error bars represent the statistical uncertainty. Periods with shattering artifacts are identified in PHIPS aspherical concentrations with grey color and for these periods the ice concentration, ice effective diameter, IWC and ice extinction coefficient are calculated only using CIP.

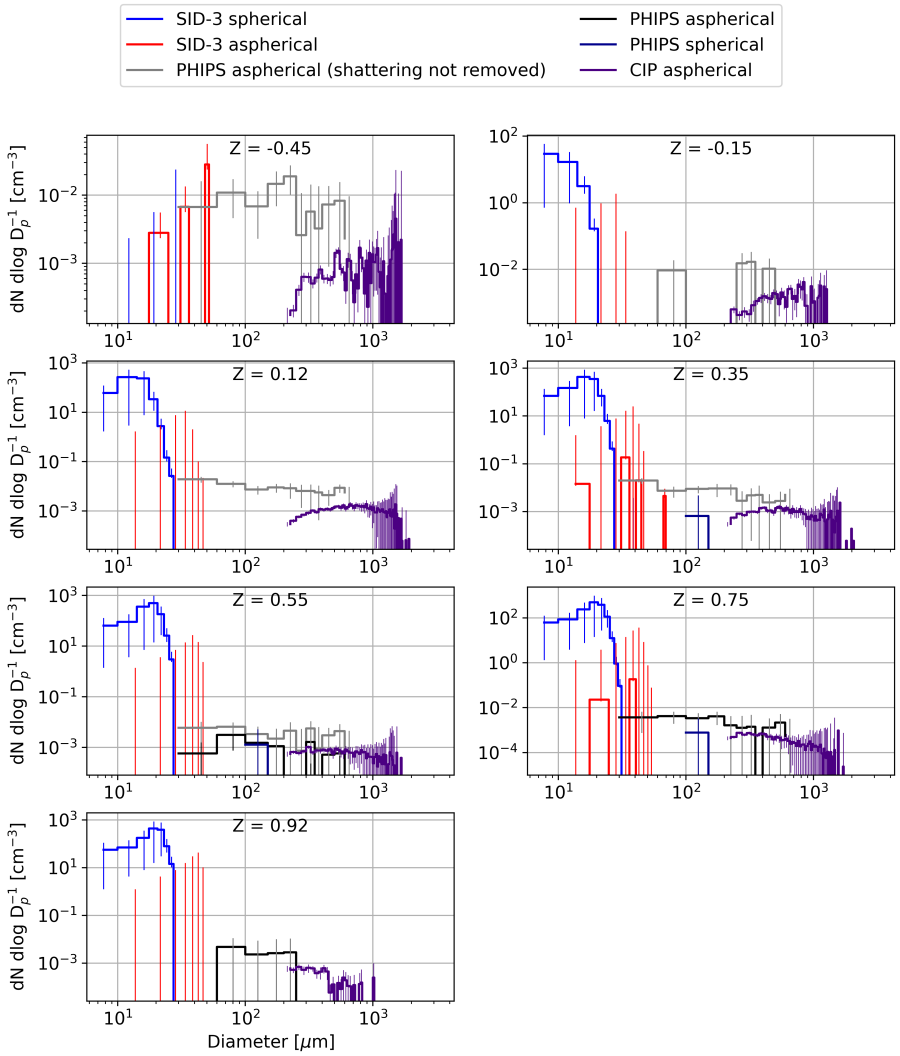

Figure S28: Phase separated particle size distributions for different normalised altitudes (Z) measured during cloud sampling on 5 June. Each sub-plot represents the particle size distributions that are averaged over one normalised altitude bin, where Z is the bin mean normalised altitude. The vertical error bars represent the statistical uncertainty. Periods with shattering artifacts are identified in PHIPS aspherical concentrations with grey color and for these periods the ice concentration, ice effective diameter, IWC and ice extinction coefficient are calculated only using CIP.

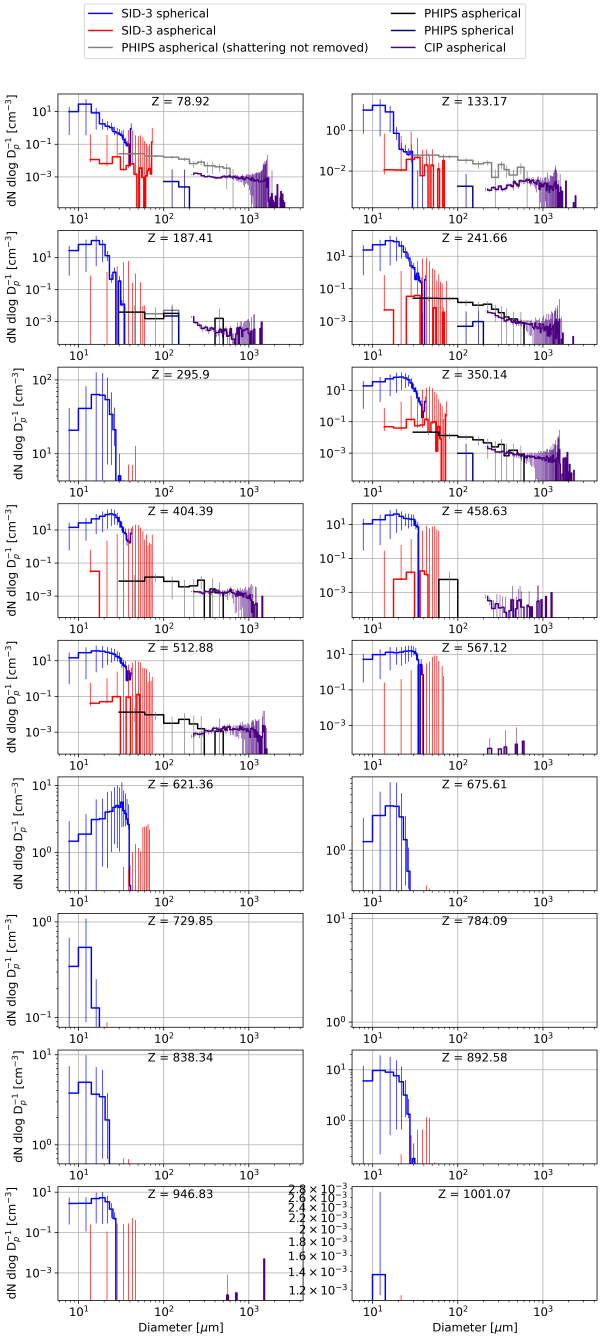

Figure S29: Phase separated particle size distributions for different altitudes (Z) measured during cloud sampling on 17 June. Each sub-plot represents the particle size distributions that are averaged over one height bin, where Z is the bin mean height in meter. The vertical error bars represent the statistical uncertainty. Periods with shattering artifacts are identified in PHIPS aspherical concentrations with grey color and for these periods the ice concentration, ice effective diameter, IWC and ice extinction coefficient are calculated only using CIP.

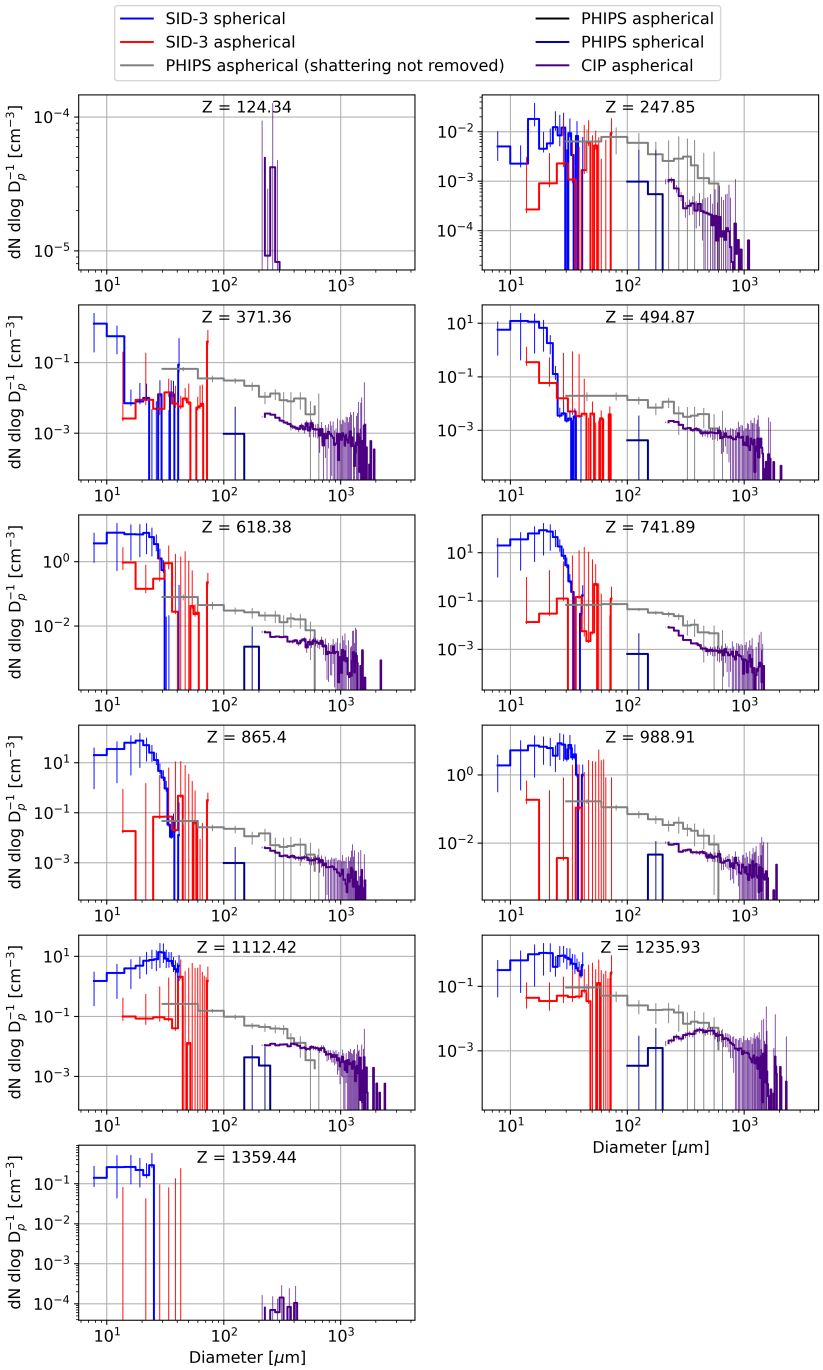

Figure S30: Phase separated particle size distributions for different altitudes (Z) measured during cloud sampling on 18 June. Each sub-plot represents the particle size distributions that are averaged over one height bin, where Z is the bin mean height in meter. The vertical error bars represent the statistical uncertainty. Periods with shattering artifacts are identified in PHIPS aspherical concentrations with grey color and for these periods the ice concentration, ice effective diameter, IWC and ice extinction coefficient are calculated only using CIP.

Table S1: Vertical cloud profiles included in the analysis of liquid water path (LWP) and ice water path (IWP) over different surfaces. For each profile the cloud top temperature (T), LWP, IWP and surface are given.

Date	Cloud Top T °C	LWP $g\,m^{-2}$	IWP $g\,m^{-2}$	surface
Cold Period				
27 May	-15.2	40.3	0.9	marginal sea ice
Warm Period				
2 June	-4.6	82.5	9.5	sea ice
4 June	-6.7	57.5	4.1	sea ice
5 June	-6.5	48.0	6.8	sea ice
8 June	-1.5	59.0	0	open ocean
8 June	-6.8	38.5	0.01	sea ice
Normal Period				
14 June	-3.8	25.6	0.5	sea ice
14 June	-3.0	14.5	0.4	sea ice
16 June	-8.7	37.6	6.0	sea ice
17 June	-5.2	31.4	8.8	sea ice
17 June	-5.1	5.5	0.0	sea ice
17 June	-2.4	90.1	0.1	open ocean
18 June	-3.0	11.8	0.01	sea ice
18 June	-3.4	21.5	0.01	sea ice
18 June	-5.3	22.7	43.7	open ocean

References

Matthew P. Bailey and John Hallett. A comprehensive habit diagram for atmospheric ice crystals: Confirmation from the laboratory, airs ii, and other field studies. *Journal of the Atmospheric Sciences*, 66(9):2888 – 2899, 2009. doi: 10.1175/2009JAS2883.1. URL `https://journals.ametsoc.org/view/journals/atsc/66/9/2009jas2883.1.xml`.

Philip R. A. Brown and Peter N. Francis. Improved measurements of the ice water content in cirrus using a total-water probe. *Journal of Atmospheric and Oceanic Technology*, 12(2):410 – 414, 1995. doi: 10.1175/1520-0426(1995)012¡0410:IMOTIW¿2.0.CO;2.

Katsuhiro Kikuchi, Takao Kameda, Keiji Higuchi, Akira Yamashita, et al. A global classification of snow crystals, ice crystals, and solid precipitation based on observations from middle latitudes to polar regions. *Atmospheric research*, 132:460–472, 2013.

R. Paul Lawson and Brad A. Baker. Improvement in determination of ice water content from two-dimensional particle imagery. Part II: Applications to collected data. *Journal of Applied Meteorology and Climatology*, 45(9):1291–1303, 2006. ISSN 15588424. doi: 10.1175/JAM2399.1.

Greg M. McFarquhar, Gong Zhang, Michael R. Poellot, Gregory L. Kok, Robert McCoy, Tim Tooman, Ann Fridlind, and Andrew J. Heymsfield. Ice properties of single-layer stratocumulus during the Mixed-Phase Arctic Cloud Experiment: 1. Observations. *Journal of Geophysical Research Atmospheres*, 112(24):1–19, 2007. ISSN 01480227. doi: 10.1029/2007JD008633.

David L. Mitchell, Renyi Zhang, and Richard L. Pitter. Mass-dimensional relationships for ice particles and the influence of riming on snowfall rates. *Journal of Applied Meteorology and Climatology*, 29(2):153 – 163, 1990. doi: https://doi.org/10.1175/1520-0450(1990)029¡0153:MDRFIP¿2.0.CO;2.

Ukitirô Nakaya and Yatarô Sekido. General classification of snow crystals and their frequency of occurrence. *Bulletin of the Faculty of Science*, 1(9):243–264, 1936.